Natural Hazards (2024) 120:2571–2597
https://doi.org/10.1007/s11069-023-06294-2

ORIGINAL PAPER

Physical vulnerability of reinforced concrete buildings under debris avalanche impact based on GF-discrepancy and DEM-FEM

Jian Pu[1] · Yu Huang[1,2] · Zhen Guo[1,2] · Yandong Bi[1] · Chong Xu[3] · Xingyue Li[1,2] · Zhiyi Chen[1,2]

Received: 8 June 2023 / Accepted: 27 October 2023 / Published online: 6 December 2023
© The Author(s), under exclusive licence to Springer Nature B.V. 2023

Abstract

Debris avalanches caused by landslides often lead to building damage, and insufficient research has been conducted on the vulnerability of buildings, especially reinforced concrete (RC) buildings, to such impact disasters. A vulnerability assessment framework for a two-story RC building based on the generalized F-discrepancy (GF-discrepancy)-based point selection strategy and discrete element method (DEM)-finite element method (FEM) is proposed. Considering the randomness of granular flow, including the impact height, impact velocity, and density of particle flow, these three random variables are uniformly sampled using GF-discrepancy, obtaining a total of 134 samples. A deterministic analysis of each sample is performed to obtain the responses of the 134 samples according to the DEM-FEM coupling method, which can fully reflect the failure characteristics of RC buildings under mass flow impact. Given the quantitative vulnerability assessment, we select the inter-story displacement ratio and the displacement of walls and columns in the responses as indicators defining the damage state of the building. The former is used to evaluate the overall damage state of the building, while the latter is applied to evaluate the local damage situation of the building as a correction to the first indicator. Ultimately, the vulnerability of the building is obtained corresponding to different impact intensities related to three random variables. This method provides not only the vulnerability of RC buildings under particle flow impact but also insight into vulnerability assessments of buildings in areas that are not currently in danger of such disasters.

Keywords Physical vulnerability · RC building · Debris avalanches · GF-discrepancy · DEM-FEM

✉ Yu Huang
yhuang@tongji.edu.cn

1 Department of Geotechnical Engineering, College of Civil Engineering, Tongji University, Shanghai 200092, China

2 Key Laboratory of Geotechnical and Underground Engineering of the Ministry of Education, Tongji University, Shanghai 200092, China

3 National Institute of Natural Hazards, Ministry of Emergency Management of China, Beijing 100085, China

1 Introduction

Debris avalanches induced by landslides, containing a large number of particles and rock fragments, frequently lead to serious infrastructure damage and severe loss of life (Petley 2012; Froude et al. 2018; Ko et al. 2018; Tang et al. 2019; Cai et al. 2022a, b; Cai et al. 2022a, b; Casagli et al. 2023). For example, on December 20, 2015, the Guangming landslide in Shenzhen destroyed 33 buildings and killed nearly 80 people (Yin et al. 2016). On May 2, 2014, the Abe Barek landslide in Afghanistan caused a death toll of up to 2700 people and resulted in nearly a hundred houses being buried (Zhang et al. 2015). A landslide occurred in Diexi Mountain, Maoxian County, Sichuan Province, resulting in 83 deaths and the destruction of numerous villages and roads in 2017 (Huang et al. 2019). With global warming and the frequent occurrence of extreme weather events, the risk of future debris avalanche disasters should not be underestimated (Papathoma-Köhle et al. 2012; Thouret et al. 2020a, b). Accordingly, a suitable vulnerability assessment of buildings is conducive to both risk assessment and risk management for government and insurance companies (Papathoma-Köhle et al. 2017).

The physical vulnerability of a building influenced by debris avalanches can usually be measured in a quantitative manner via three methods: vulnerability matrices, vulnerability indicators, and vulnerability curves (Papathoma-Köhle et al. 2017; Thouret et al. 2020a, b). Vulnerability curves, the most common method of risk evaluation, define the relationship between the intensity of the debris flow, e.g., the flow depth, impact velocity, viscosity of debris, and impact pressure, and the damage response of an element; this method often requires a large amount of reliable historical statistical data collected after a debris flow event (Prieto et al. 2018; Liang et al. 2019; Luo et al. 2020; Yan et al. 2020). The data used for drawing the vulnerability curves usually come from authorities and insurance company and field investigations, which may be time-consuming and expensive. If an area likely to be impacted by future debris has not experienced a previous debris disaster, this work can be particularly difficult to perform.

Given the development of computer technology in recent years, numerical simulation methods may be able to compensate for the disadvantages that arise in the above-mentioned method because computational methods can simulate various impact scenarios for different types of buildings with different characteristics to obtain the various data required for debris flow risk analyses (Quan Luna et al. 2011; Chen et al. 2021; Qingyun et al. 2022). For example, Cheng et al. (2022) investigated the physical vulnerability of buildings to construction solid waste by evaluating the resistance of the buildings and the impact height determined by a simplified flow slide model that they developed. Similarly, Zhang et al. (2018) built a vulnerability curve using the debris intensity of the flow depth, flow velocity, and impact pressure simulated via FLO-2D at a regional scale based on a debris event that occurred in Zhouqu County, Gansu Province, Northwest China. Kim et al. (2020) also applied this software to build a vulnerability curve in Korea. These authors used numerical methods to provide accurate simulation data, saving a large amount of on-site investigation time; however, the interaction process between debris flows and buildings has been ignored to a certain extent. Interestingly, this issue attracted the attention of Luo et al. (2022), who established a simplified equivalent impact model in which the impact force is estimated via hydrodynamic models with uniform (Fig. 1a) and trapezoidal (Fig. 1b) pressure distributions (p_{slurry} and $F_{boulder}$ represent pressure of slurry and impact force of boulders), and ultimately constructed a series of fragility curves via approximately 5000 simulations in LS-DYNA, considering the uncertainties of the debris in an explicit

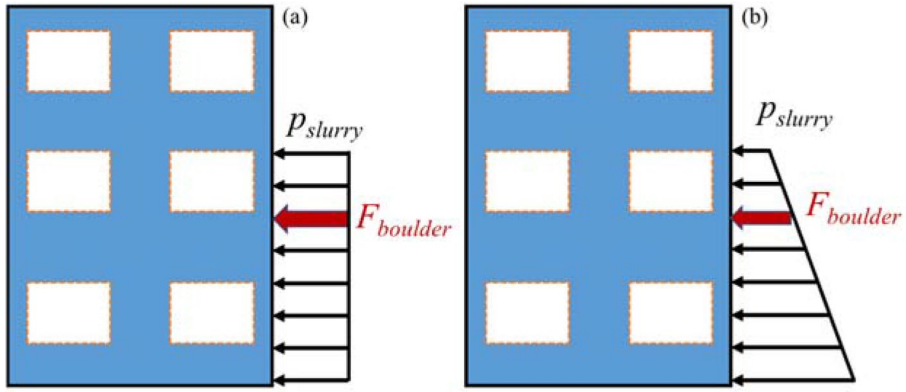

Fig. 1 Schematic diagram of simplified equivalent impact model

manner. Although interactions between debris flows and buildings have been considered, true dynamic contact models, which can accurately simulate the entire process of failure of building, have not yet been applied to vulnerability assessments of buildings impacted by debris flows because of the large computational costs, both in time and money.

Dynamic contact models can not only effectively simulate the dynamic damage process of existing buildings but also provide various data that are difficult to collect on site, and therefore applying these methods to vulnerability assessments is very beneficial (Luo et al. 2021; Yu et al. 2022). However, one important issue needs to be addressed: how can real debris flow impact scenarios, including all of types of impact cases, be selected as accurately as possible when the uncertainties of debris flows are considered (Luo et al. 2020, 2022). The most commonly used sample methods to solve this problem are Monte Carlo simulation (MCS) and Latin hypercube sampling (LHS), which has been widely used in probability analyses (Shields et al. 2016). However, MCS requires a large samples size to obtain the desired result, and if the size of samples is small, significant deviations may arise (Li et al. 2023). Although LHS can control the deviation between the sample and the population, small samples are not very uniform in the context of multidimensional variable sampling, which also lead to discrepancy in vulnerability. Due to the expensive computing cost of dynamic contact model used for evaluating vulnerability, there is not possible to calculate too many samples. Hence, these two methods are not suitable for sampling when dynamic contact models are used to investigate vulnerability.

Fortunately, a point selection method based on generalized F-discrepancy (GF-discrepancy) can deal with the problem, which was proposed by Chen et al. (2016) and improved by Yang et al. (2019). This method effectively manages the discrepancy between the sample distribution function and the population distribution function, while also producing samples that are relatively uniform, even for small samples (Chen et al. 2019). The method has been used successfully in structural fragility analysis. For example, Ren et al. (2022) built a fragility curve of a prestressed concrete containment vessel considering the uncertainties of the concrete and steel rebar, and Chen et al. (2023) explored the seismic fragility of concrete face rockfill dams, given uncertainties in the ground motions and soil variability. Furthermore, Li et al. (2023) found that, under the same sample size, the calculation results based on the GF-discrepancy method are significantly better than those based on MCS and that GF-discrepancy avoids the problem of redundant calculation experienced when using MCS. Therefore, GF-discrepancy is suitable for generating representative samples in vulnerability evaluation.

At present, the vulnerability of reinforced concrete (RC) buildings impacted by debris avalanches originating from mountain collapses or landslides has not attracted sufficient attention (Zhang et al. 2018). There are many dynamic contact models that can be used to investigate the vulnerability of RC building under mass flow impact, including discrete element method (DEM)-finite element method (FEM) (Zhong et al. 2022; Yuen et al. 2023), smooth particle hydrodynamics (SPH)-FEM (Feng et al. 2019; Liu et al. 2022), arbitrary Lagrangian–Eulerian (ALE)-FEM (Luo et al. 2019, 2021), and SPH-DEM-FEM (Liu et al. 2021; Qingyun et al. 2022). In these methods, the deformation and failure of RC building are calculated by FEM, while the debris flow is simulated using DEM, SPH, or ALE. Compared with SPH-FEM, ALE-FEM, and SPH-DEM-FEM, DEM-FEM is more suitable for vulnerability studies because the other methods are highly time-consuming. In addition, DEM-FEM has been successfully applied to the study of bridge pier failure under impact of particle flow (Zhong et al. 2022). Accordingly, the DEM-FEM coupling method is chosen in this study to explore the vulnerability of RC buildings impacted by dry grain flows.

Here, explicitly considering the randomness of debris avalanches, including the impact height, impact velocity, and density of particle flow, 134 representative samples are sampled in accordance with GF-discrepancy. Subsequently, a deterministic analysis is performed on the 134 samples in LS-DYNA based on DEM-FEM to obtain the dynamic responses of these cases. Furthermore, quantitative building damage states are proposed according to the inter-story drift ratio and the damage degree of the walls and columns of an RC building and vulnerability curves related to different impact intensity indicators are established based on the Weibull distribution. Finally, we compare the vulnerability curves derived from debris avalanches with those of common debris flows.

2 Method

2.1 Point selection method based on GF-discrepancy

To control the uniformity of the sampling points used in the vulnerability analysis, the sampling discrepancy of the sampling points needs to be controlled; that is, to reduce the discrepancy between the empirical distribution function and the cumulative distribution function (CDF) of the samples. The discrepancy of the CDF can be controlled by the discrepancy of the joint probability density function (PDF), and the PDF can be expressed by a combination of the moments of the characteristic function. Therefore, if the error of each central moment is small, the error of the distribution function is also small. For n-dimensional random variables $\Theta = \left(\Theta_1, \Theta_2, \cdots, \Theta_n\right)$, the worst error D_α of its n-th central moment can be expressed as (Li et al. 2017)

$$D_\alpha = \left| \int_{\Omega_\Theta} f_\alpha(\theta, t) p_\Theta(\theta) d\theta - \sum_{q=1}^{n} P_q f_\alpha(\theta, t) \right| \leq V_{EF}\left(f_\alpha\right) D_{EF}\left(\mathfrak{R}_n\right), \tag{1}$$

$$\mathfrak{R}_n = \left\{ \theta_q = \left(\theta_{q,1}, \theta_{q,2}, \cdots, \theta_{q,s}\right), q = 1, 2, \cdots, n \right\}, \tag{2}$$

where $D_{EF}\left(\mathfrak{R}_n\right)$ and Ω_Θ are the extended F-discrepancy of the point set $\mathfrak{R}_n$ and the range space of a random variable Θ, respectively; s is the dimension unit hypercube. $f_\alpha(\theta, t)$ is a function with bounded variation whose expression is generally unknown; $p_\Theta(\theta)$ is the joint PDF of the random variable Θ; $V_{EF}\left(f_\alpha\right)$ is the total variation of the function f_α; and P_q is the probability calculated according to a Voronoi cell.P_q can be calculated by Eq. (3) and $D_{EF}\left(\mathfrak{R}_n\right)$ is both defined by Eq. (4) and depicted in Fig. 2 (Chen et al. 2013).

$$P_q = \int_{\Omega_q} p_\Theta(\theta) d\theta, \tag{3}$$

$$D_{EF}\left(\mathfrak{R}_n\right) = \sup \left| F_n\left(\theta, \mathfrak{R}_n\right) - F_n(\theta) \right| \quad \left(\theta \in \Omega_\Theta\right), \tag{4}$$

where $F_n(\theta)$ and $F_n\left(\theta, \mathfrak{R}_n\right)$ are the joint CDF of the random variable Θ and the empirical CDF determined by the assigned probabilities of the point set $\mathfrak{R}_n$, respectively. $F_n\left(\theta, \mathfrak{R}_n\right)$ can be expressed as

$$F_n\left(\theta, \mathfrak{R}_n\right) = \sum_{q=1}^{n} P_q I\left\{\theta_q \le \theta\right\}. \tag{5}$$

Here, $I\left\{\theta_q \le \theta\right\}$ is the indicator function, which is 1 when the expression is true and 0 when it is false. It is difficult to determine an analytical expression of Eq. (1), making it difficult to solve. To avoid this NP-hard problem, the GF-discrepancy method based on the marginal PDF is proposed, as defined in Eq. (6).

$$D_{GF} = \max_{1 \le j \le s} \left\{ \sup_{-\infty \le \theta_j \le \infty} \left\{ \left| F_{n,j}\left(\theta_j, \mathfrak{R}_n\right) - F_{n,j}\left(\theta_j\right) \right| \right\} \right\} \tag{6}$$

Here, $F_{n,j}\left(\theta_j\right)$ and $F_{n,j}\left(\theta_j, \mathfrak{R}_n\right)$ are the marginal CDF and the empirical marginal CDF of the j-th random variable, respectively. It has been proven that there exists a constant s that leads to the following relationship between D_{GF} and D_{EF}:

$$D_{GF}\left(\mathfrak{R}_n\right) \le D_{EF}\left(\mathfrak{R}_n\right) \le sD_{GF}\left(\mathfrak{R}_n\right). \tag{7}$$

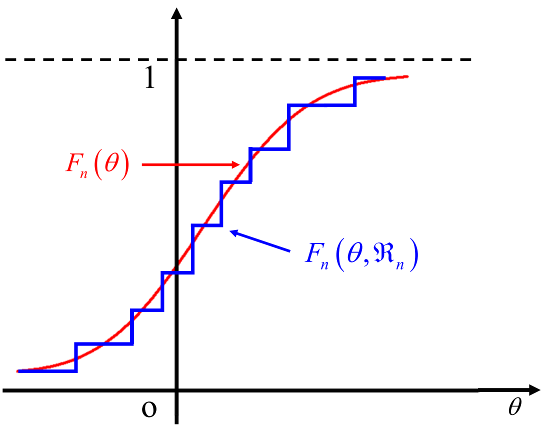

Fig. 2 Schematic diagram of the total discrepancy D_{EF} for a one-dimensional distribution

According to Eq. (7), Eq. (1) can be rewritten as

$$\left| \int_{\Omega_\Theta} f_\alpha(\theta,t) p_\Theta(\theta) d\theta - \sum_{q=1}^{n} P_q f_\alpha(\theta,t) \right| \le s V_{EF}\left(f_\alpha\right) D_{GF}\left(\mathfrak{R}_n\right). \tag{8}$$

Equation (8) indicates that the total discrepancy D_{EF} of the system can be controlled by reducing the marginal discrepancy D_{GF}, such that, not only can n-dimensional problems be simplified to one-dimensional problems but also a relatively uniform point set can be obtained by assigning approximately equal probability. A uniform point set can be achieved via the Sobol sequence method, which first generates a Sobol sequence containing n random variables, where each dimension of the variable follows a uniform distribution with a minimum of 0 and a maximum of 1. The Sobol sequence can be expressed as $\mathfrak{R}_{n,sob} = X_{ns}$. Then, according to the inverse function of the CDF, inverse transformation can be performed on the point set $\mathfrak{R}_{n,sob}$ to obtain the initial point set $\theta_{q,j}$:

$$\theta_{q,j} = F_j^{-1}\left(x_{q,j}\right) \quad (q \in [1,n]; j \in [1,s]). \tag{9}$$

where $F_i(\cdot)$ is the marginal CDF of j-th random variable.

$\mathfrak{R}_{n,sob}$ is not absolutely uniform, and therefore the initial point set obtained via Eq. (9) is the same, such that the assigned probability of each point being partitioned by the Voronoi cell is uneven. Therefore, the point set $\theta_{q,j}$ needs to be rearranged; this can be divided into two steps. First, the position of the initial point set is rearranged to make the assigned probability of each point as close as possible, which can be adjusted according to Eq. (10). Then, the point set is adjusted using Eq. (11) based on the Voronoi partitioning method to minimize its GF-discrepancy. The point set adjusted via these two steps is a relatively uniform point set. Equations (10) and (11) are as follows (Yang et al. 2019):

$$\theta_{q,j}^1 = F_j^{-1}\left[\sum_{k=1}^{n} \frac{1}{n} I\left(\theta_{k,j} < \theta_{q,j}\right) + \frac{1}{2n}\right], \tag{10}$$

$$\theta_{q,j}^2 = F_j^{-1}\left[\sum_{k=1}^{n} P_q I\left(\theta_{k,j}^1 < \theta_{q,j}^1\right) + \frac{1}{2} P_q\right]. \tag{11}$$

2.2 DEM-FEM coupled model

DEM is a common numerical method widely used in the study of solid particles, especially debris, and its principle is shown in Fig. 3a. In this method, particles of different sizes are modeled by soft balls allowing slight penetration in order to transfer forces between particles. The translation and rotation between particles follow Newton's second law, and the motion control and momentum conservation equations of the particles are (Liu et al. 2021; Zhong et al. 2022)

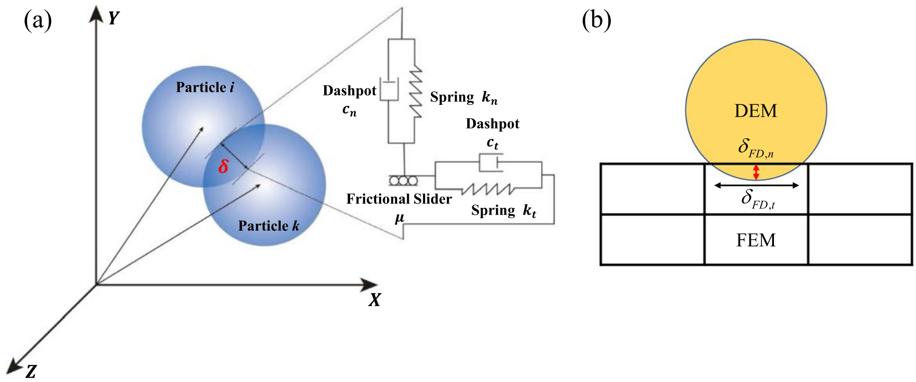

Fig. 3 Contact model of DEM **a** and DEM-FEM **b** (Liu et al. 2019)

$$\begin{cases} m_i \ddot{\mu}_i = m_i g + \sum_{k=1}^{s} (f_{n,ik} + f_{t,ik}) \\ I_i \ddot{\theta}_i = \sum_{k=1}^{s} T_{ik} \end{cases}, \tag{12}$$

where m_i, $\ddot{\mu}_i$, $\ddot{\theta}_i$, and I_i are the mass, translation acceleration, rotational acceleration, and moment of inertia of the i-th particle, respectively; $f_{n,ik}$, $f_{t,ik}$, and T_{ik} denote the normal contact force, tangential contact force, and torque, respectively, between the i-th and k-th particle; and g and s are the gravitational acceleration and the total number of particles in contact with the i-th particle, respectively.

In Eq. (12), the magnitude of the contact force calculated based on the linear spring dashpot model is related to the overlap thickness between the soft balls and the magnitude of the contact velocity. Specifically, the tangential contact force between the particles follows Coulomb's law of friction. The expressions for the overlap thickness between the particles δ, normal contact force $f_{n,ik}$, and tangential contact force $f_{t,ik}$ are

$$\delta = r_i + r_k - |X_i - X_k|, \tag{13}$$

$$f_{n,ik} = (-k_n \delta_n + c_n \dot{\delta}_n), \tag{14}$$

$$f_{t,ik} = \min(-k_t \delta_t + c_t \dot{\delta}_t,\ u f_{n,ik}), \tag{15}$$

where r_i and X_i are the radius and a vector showing the position of the i-th particle, respectively; k_n, δ_n, $\dot{\delta}_n$ and c_n represent the normal spring stiffness, normal overlap thickness, normal relative velocity, and normal damping coefficient, respectively; and $k_t, \delta_t, \dot{\delta}_t, c_n, u$ are the tangential spring stiffness, tangential overlap, tangential relative velocity, tangential damping coefficient, and friction coefficient, respectively. Here, k_n, k_t, c_n, c_t can be defined by (Karajan et al. 2014)

$$k_n = \frac{\kappa_i r_i \kappa_k r_k}{\kappa_i r_i + \kappa_k r_k} n_n,\ k_t = k_n n_t, \tag{16}$$

$$c_n = 2\eta_n \sqrt{\frac{m_i m_k}{m_i + m_k} k_t},\ c_t = 2\eta_t \sqrt{\frac{m_i m_k}{m_i + m_k} k_n}, \tag{17}$$

where κ_i represents the bulk modulus of the i-th particle, which is equal to $E/3(1-2v)$; n_n and n_t are ratio constants of the normal and tangential stiffness, which are generally taken to be 0.01 and 2/7 (Albaba et al. 2017; Liu et al. 2019), respectively; and η_n and η_t represent the normal and tangential damping ratios, respectively, between the particles.

A coupling diagram of DEM and FEM is shown in Fig. 3b, and the motion between DEM and FEM satisfies Eq. (18), where the first two equations are the DEM control equations and the final equation is the FEM control equation (Liu et al. 2021; Zhong et al. 2022).

$$\begin{cases} m_i \ddot{\mu}_i = m_i g + \sum_{k=1}^{s} (f_{n,ik} + f_{t,ik}) + \sum_{j=1}^{l} (f_{n,ij} + f_{t,ij}) \\ I_i \ddot{\theta}_i = \sum_{k=1}^{s} T_{ik} + \sum_{j=1}^{l} T_{ij} \\ M\ddot{X} + C\dot{X} + KX = F_{\text{contact}} + F_{\text{non\_contact}} \end{cases} \tag{18}$$

Here, $f_{n,ij}$, $f_{t,ij}$ and T_{ij} are the normal contact force, tangential contact force, and torque, respectively, between the i-th discrete element and the j-th finite element; l is the number of finite elements in contact with discrete elements;X, M, C and K denote the displacement matrix, mass matrix, damping matrix, and stiffness matrix, respectively, of the finite element set; $F_{contact}$ represents the external force imposed by the discrete element; and $F_{non\_contact}$ represents external force other than contact force applied by discrete element.

The contact force between DEM and FEM is determined based on a penalty function, and similar to Eqs. (14) and (15), the magnitude of the contact force is also related to the stiffness of the contact spring, penetration depth, and relative velocity. $f_{n,ij}$ and $f_{t,ij}$ can be expressed as

$$f_{n,ij} = \left(-k_{FD,n}\delta_{FD,n} + c_{FD,n}\dot{\delta}_{FD,n}\right), \tag{19}$$

$$f_{t,ij} = \min\left(-k_{FD,t}\delta_{FD,t} + c_{FD,t}\dot{\delta}_{FD,t}, uf_{n,ij}\right), \tag{20}$$

where $\dot{\delta}_{FD,n}$ and $\dot{\delta}_{FD,t}$ represent the normal and tangential penetration thicknesses, respectively, between DEM and FEM; $c_{FD,n}$ and $c_{FD,t}$ are the normal and tangential damping coefficient, respectively, commonly set to 0 in the absence of high-frequency oscillations; and $k_{FD,n}$ and $k_{FD,t}$ refer to the stiffnesses of the normal contact spring and the tangential spring on the contact surface between finite and discrete elements, which are usually assumed to be equal. The contact spring stiffness expressions for DEM with shell elements and solid elements are (Liu et al. 2021)

$$k_{FD,n} = \max\left[\frac{l_{SOFSCL} m}{2\Delta(t)}, \frac{k_{penalty} KA}{\max(\text{shell diagonal})}\right], \tag{21}$$

$$k_{FD,n} = \max\left[\frac{l_{\mathrm{SOFSCL}}m}{2\Delta(t)}, \frac{k_{\mathrm{penalty}}KA^2}{V}\right], \tag{22}$$

where l_{SOFSCL} and $k_{penalty}$ are the scale factor of the soft constraint penalty formulation and the penalty scale factor for the contact spring stiffness, respectively, with l_{SOFSCL} and $k_{penalty}$ set to 0.1 meeting most computational needs; K and $\Delta(t)$ are the bulk modulus of the finite element and the time step function, respectively; m is a function of the slave node set of the discrete element and the master node set of the finite element on the contact surface; A and V are the surface area and volume of the finite element, respectively.

2.3 Material models

The cap model, which considers the hardening and damage of concrete materials, is widely used in the progressive collapse of buildings in impact debris flows and has achieved good simulation results (Luo et al. 2019). This model realizes a smooth connection between the shear failure surface and the hardened cap surface, solving the numerical calculation problem caused by the discontinuity between the two. The yield surface equation is (Murray 2007)

$$f(J_1, J_2, J_3, k) = J_2 - R^2F_f^2\left(J_1\right)F_c\left(J_1, k\right), \tag{23}$$

where J_1, J_2 and J_3 are the first invariant of the stress tensor and the second and third invariants of the deviatoric stress tensor, respectively; R and k are the strength reduction coefficient and cap hardening parameter, respectively, of concrete. $F_f\left(J_1\right)$ and $F_c\left(J_1, k\right)$ represent the shear failure surface equation and the hardening cap equation, respectively, and are expressed as

$$F_f(J_1) = \alpha - \lambda e^{-bJ_1} + \varphi J_1, \tag{24}$$

$$F_c(J_1, k) = 1 - \frac{\left[J_1 - L(k)\right]\left[|J_1 - L(k)| + J_1 - L(k)\right]}{2[X(k) - L(k)]^2}, \tag{25}$$

where α, e, b and φ are fitting parameters of the failure surface determined via uniaxial compression experiments on plain concrete; $X(k)$ and $L(k)$ are operator functions related to the hardening parameters. The cap model generally determines its failure based on its maximum principal strain, and when the maximum principal strain exceeds 0.05 (the default value), it is determined that the concrete element is to be deleted.

Reinforcement in concrete usually follows the elastic–plastic constitutive law (Shi et al. 2021), which can accurately describe the hardening behavior of the reinforcement after being stressed. Its constitutive equation is

$$\sigma_y = \left(\sigma_0 + \beta E_p\varepsilon_p^e\right)\left[1 + \left(\frac{\dot{\varepsilon}}{C}\right)^{(1/P)}\right]. \tag{26}$$

Here, σ_0 is the initial stress; E_p, β are the hardening modulus and the hardening parameters, respectively; ε_p^e and $\dot{\varepsilon}$ the effective strain and the strain rate, respectively. C and P refer to the strain rate parameter. Parameters related to strain rate maintains the default value during calculation.

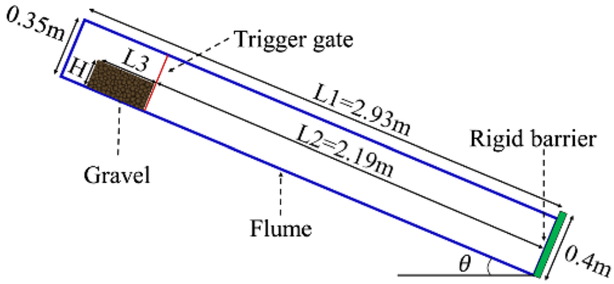

Fig. 4 Schematic diagram of the flume test

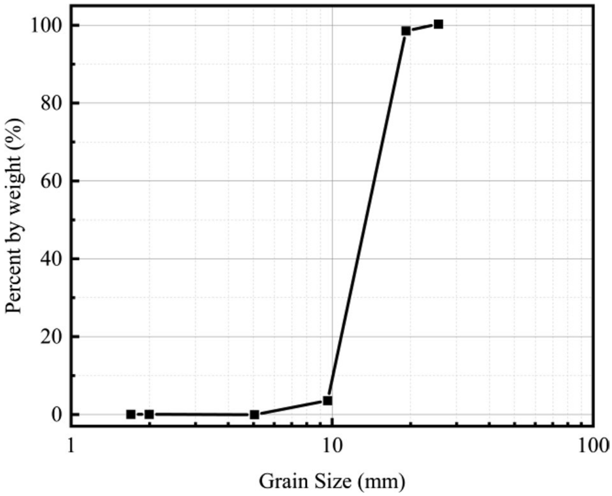

Fig. 5 Particle size distribution

2.4 Experimental validation

To verify the effectiveness of DEM-FEM, we selected a flume test of a debris avalanche as a reference (Jiang et al. 2013). This test is treated as a benchmark to calibrate the DEM parameters because there are no experiments in which particles directly impact concrete. The flume test system is 2.93 m long (L1), 0.3 m wide, and 0.35 m high, as shown in Fig. 4, with a 0.4-m rigid barrier equipped with force sensors at the bottom of the system. The sliding mass, with a length of 0.44 m (L3), width of 0.3 m, and height of 0.15 m (H), slides down a 50° (θ) flow channel and impacts the rigid barrier at a distance of 2.19 m (L2). The bulk density of the sliding mass is 1350 kg/m^3, having a corresponding particle density of 2800 kg/m^3. Particles having a distribution of 10–20 mm account for over 95% of the total according to Fig. 5; therefore, the particle size is set to 10–20 mm in the simulation. The normal and tangential damping coefficients of the particles are set to 0.9 and 0.3, respectively. The friction coefficients between the particles and the floor, the sidewall, and the rigid barrier of the flume are 0.38, 0.55, and 0.38, respectively. The grain, flume, and barrier materials are treated as rigid, rigid, and elastic, respectively. The particles and the barrier and the particles and the flume have automatic node to surface contacts between them. The simulation was performed using LS-DYNA, and the simulation parameters are given in Tables 1 and 2.

Table 1 Parameters of the discrete element particles

Bulk density	c_n	c_t	n_n	n_t	Friction coefficient	Rolling friction coefficient
1350 kg/m^3	0.9	0.3	0.01	0.0029	1.4	0.12

Table 2 Material parameters of the different parts of the simulation

Element	Nature	Density (kg/m^3)	Elastic modulus (GPa)	Poisson's ratio
Particle	rigid	2800	30	0.3
Flume	rigid	7850	30	0.3
Barrier	elastic	7850	200	0.25

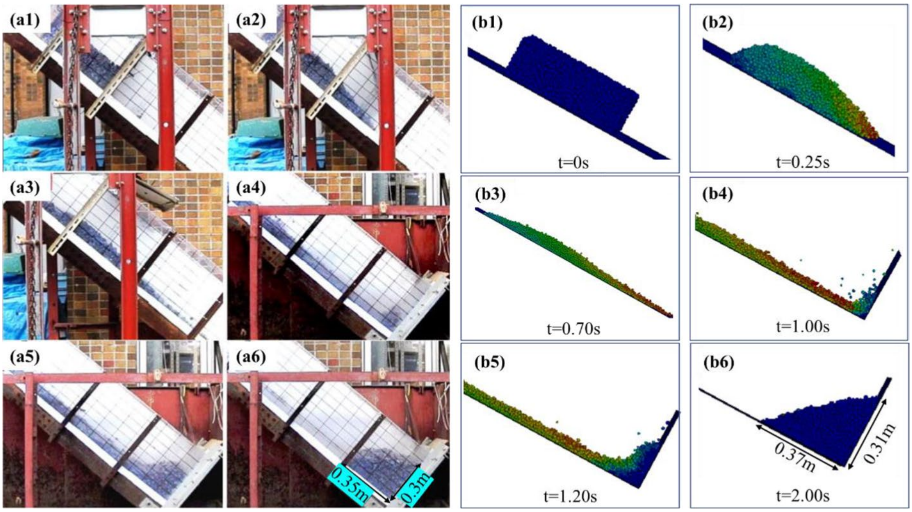

Fig. 6 Flow state verification of the numerical model and flume tests: **a1**–**a6** flume test of Jiang et al. (2013) and **b1**–**b6** simulation results

Comparisons between the flume test and the numerical simulation are shown in Fig. 6 and Fig. 7. Figure 6a1–a5 and b1–b5 shows that the flow state of the simulation matches that of the experiment quite well at different times; the stacking state Fig. 6a6–b6 is also the same. Figure 6a6–b6 indicates that the errors of the stacking lengths parallel and perpendicular to the blocking structure are 5.7% and 3.33%, respectively. Similarly, Fig. 7 shows that the deviation of the normal impact force is approximately 3% after the original impact force data are smoothed via a fast Fourier transform (FFT). Overall, the accurate calculation results, for both the flow state and the impact force, indicate that particles simulated based on DEM can make good contact with the flume and retaining structure based on FEM, and that these methods are capable of simulating the impact process of a debris avalanche.

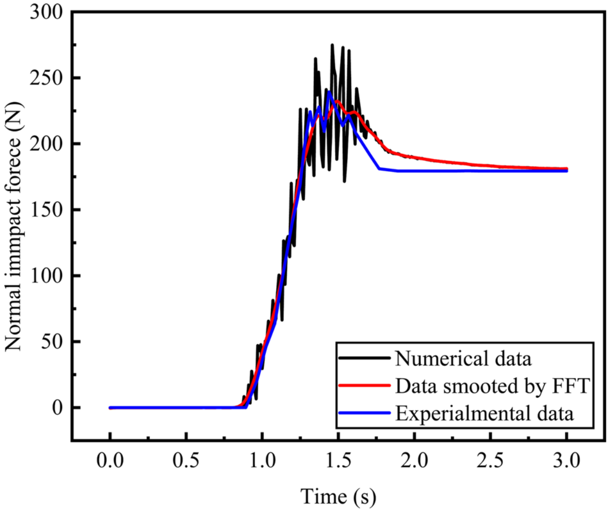

Fig. 7 Impact force comparison of the numerical model and flume test

3 Numerical model

To construct a model with strong transferability, the randomness of not only the debris flows but also the buildings needs to be considered. The randomness of an architectural structure primarily arises from the materials, dimensions, and geometric shape of the building (Kappes et al. 2012). However, dividing the finite element models of building are very challenging when the randomness of building is considered. Therefore, this randomness is overlooked in our research. To make the research more meaningful, the two-story RC building with common features in rural areas of China is selected as the analysis objects. Papathoma-Köhle et al. (2017) thought that the complete destruction of the structure of a building is only caused by a frontal debris flow impact; therefore, we primarily consider frontal impacts of the representative building in this article.

The numerical model of the two-story RC building is shown in the blue box in the upper left corner of Fig. 8; the length of the debris flow is 3 m, as determined by trial and error to ensure a sufficient impact force, the width of the debris flow is 3.15 m, corresponding to the width of the building, and the height of the debris flow is an unassigned random variable. The length, width, and height of the building placed on a foundation, are 6.4 m, 3.15 m, and 5.9 m, respectively. A total of 12 longitudinal steel bars with a diameter of 14 mm are evenly arranged in beam sections and column, with a length of 40 mm, and are reinforced by stirrups with a diameter of 10 mm. In the non-encrypted area (yellow box), the spacings between the stirrups placed in the beams and column are 20 cm and 15 cm, respectively, while in the encrypted area (purple box), the spacing between the stirrups is 10 cm. The walls and floor, with thicknesses of 20 cm and 10 cm, respectively, contain double-layer rebar with a diameter of 10 mm and spacings of approximately 25 cm and 15 cm, respectively. Three monitoring lines are set up on the building to detect the displacements on the column (Line A), impact face (Line B), and far end of the column (Line C). In this study, the concrete protective layer of the steel bar is set to 25 mm. These parameters are mainly determined by engineering experience and Code for Seismic Design of Buildings (2016).

The parameters of the particle flow are basically consistent with those in Table 1, and the values of the density, impact height, and impact velocity of the granular flow are

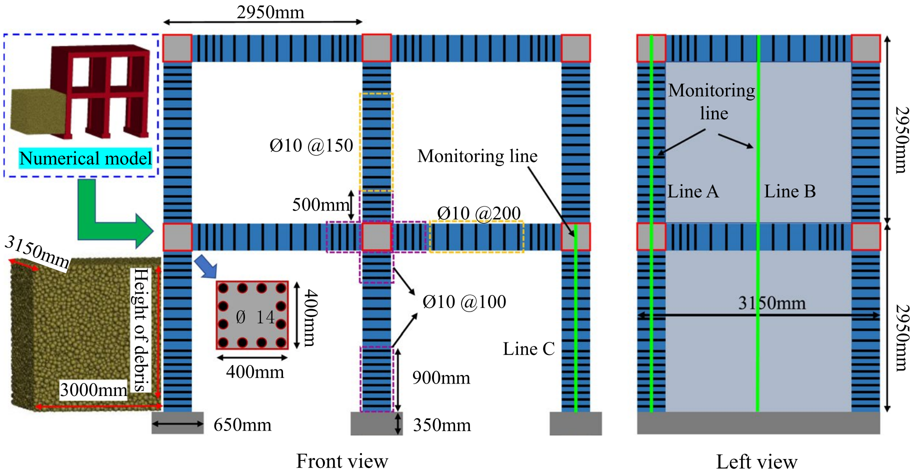

Fig. 8 Schematic diagram of the dynamic impact model

given in Sect. 4. The rebars are modeled using a beam with a Hughes–Liu cross section, and the rebar parameters are listed in Table 3 in which an average yield strength value of 455.7 MPa corresponds to a standard yield strength value of 400 MPa with a guarantee rate of no less than 95%. The concrete is modeled using constant stress elements, and the concrete parameters of the cap model, except for the average compressive strength, which is set to 28 MPa, adopt the default values listed in Table 4. The interaction of the rebars and concrete is modeled using the constrained_beam_in_solid algorithm, and the contacts of the particles with the beams and concrete are characterized using the de_to_beam_coupling and eroding_nodes_to_surface algorithms, which describe the erosion of the discrete particles on the finite elements of the concrete. This study assumes that the foundation does not experience any displacement, and therefore that full constraints are applied to the foundation.

4 Sampling based on GF-discrepancy

In general, a large number of random variables are involved in a vulnerability assessment, of which the factors related to the impact force of the debris are easier to consider; these include the velocity, height, and density of the debris avalanche. The velocities of debris avalanches produced by landslides range from several meters per second to hundreds of meters per second; we only consider impact situations with relatively low mass flow speeds because of the strong destructive nature of high-speed debris flows. The velocity and height of a debris event in a flow channel are generally assumed to follow a uniform distribution (Luo et al. 2022), with the velocity range a debris flow being 1–12 m/s (Table 5). Usually, when the height of a debris flow exceeds the height of the building, resulting in the building being completely buried, it is assumed that the building is completely destroyed, losing its value in the vulnerability assessment. In addition, if the depth of the debris flow is too shallow, it is assumed to not have a significant impact force, thus not causing any damage to the building. Accordingly, the depth of the debris flow was set to be between 1 m and 5.9 m (Table 5). As for the density, numerous studies have shown that the density follows

Table 3 Parameters of rebars with different diameters

Diameter (mm)	Density (kg/m3)	Young's modulus (GPa)	Poisson's ratio	Yield stress (MPa)	Tangent modulus (MPa)	Failure strain	β
ϕ14/ϕ10	7850	200	0.3	455.7	2000	0.1	0

a logarithmic normal distribution; in this study, we assumed that the mean of density of flowing material was 1800 kg/m^3 with a coefficient of variation of 5%, following the study of Parisi et al. (2017) (Table 5).

According to the research of Papathoma-Köhle et al. (2017), the number of damaged buildings typically used in existing vulnerability curves is in the tens. We are confident that offering over 100 cases with different damage states can fulfill the demand of the statistical analysis of vulnerability. Finally, approximately 134 samples are selected based the point selection strategy of GF-discrepancy for the consideration of balancing calculation time and accuracy of vulnerability. The PDFs and CDFs of the velocity (v), height (h), and density (ρ) of the selected samples according to Eqs. (9–11) are shown in Fig. 9. Known from Fig. 9, the selected points are basically uniformly distributed in their range spaces, with small PDF deviations. After trial and error calculations, we found that the entire model only requires 0.15 s of calculation time to ensure that the building reaches its maximum displacement if the displacement rebounds; therefore, the termination time for all models was set to 0.15 s.

5 Definition of building damage states

Definitions of the different levels of vulnerability of a building often vary across study areas and for different types of buildings, the classification of damage states is often qualitative, as shown in Table 6. Table 6 defines the level of vulnerability from a macro perspective; however, when this definition is used to determine the damage states of buildings in numerical models, if there are many models, non-quantitative evaluation methods have extreme difficulty achieving statistical analyses. Consequently, quantitative evaluation indictors within the framework of macro definitions are urgently needed.

Here, inspired by the failure modes of RC buildings under earthquake excitation, we propose a quantitative classification of building damage levels based on failure modes to increase the transferability of the evaluation method. The failure modes of an RC building impacted by granular flow at the current reinforcement ratio are shown in Fig. 10. Regardless of the height of the debris flow, the entire building tends to move in the same direction as the debris flow, which leads to rupture of the building's beam column joints (within the red box). Because the foundation of the building is assumed to be immovable, movement of its upper structure is equivalent to generating inter-story drift ratio. Accordingly, the overall damage status of the building can be determined by the inter-story drift ratio of the columns at the farthest end from the debris flow. This determination is generally correct; however, further correction is still needed. For example, the inter-story drift ratio correctly determines the failure state for Fig. 10a but is not applicable to Fig. 10b because there is no significant destroy signal at the far end, rather the elements on the impact surface

Table 4 The parameters of concrete of cap model

Density (kg/m^3)	Compressive strength (MPa)	Failure strain	Maximum aggregate size (mm)
2500	28	0.05	18

Table 5 Probability distribution of random variables

Variable	Lower interval/mean	Upper interval/CoV	Distribution
Velocity (v)	1m/s	12m/s	Uniform
Height (h)	1m	5.9m	Uniform
Density (ρ)	1800kg/m^3	3%	Lognormal

are completely destroyed. Therefore, in addition to considering the overall damage of the building, the local damage of the beams and columns on the contact surface needs to be considered.

Based on Table 6, a quantitative definition of RC building damage considering both overall (Condition A) and local (Condition B) building damage state is shown in Table 7. In the table, δ is the inter-story drift ratio at the farthest, characterizing the overall degree of damage of the building, whose value is referring to Code for Seismic Design of Buildings (2016). Furthermore, to solve the problem of insufficient description of local damage by δ, two indicators of D_{wall} and D_{column} representing local damage of buildings are proposed. D_{wall} and D_{column} mean the displacements of the foot of the wall and column first collided with debris flow, and their values are summarized from numerical models without a unified reference. In our simulation, when D_{wall} reaches 0.001m, the wall cracks, and when D_{column} is 0.01 m, the column begins to shear failure; when D_{column} reaches to 0.4m, the column loses its support capacity and detaches from its original position. Here, we use an example to illustrate the meaning of Table 7. If the displacement at the far end of a building falls within the range from 1/550 to 1/100 (Condition A), it is considered to be in a state of slight damage that will be further evaluated based on the displacement of the column at the impact face (Condition B). Then, if the displacement of the column exceeds 0.01 m, the final damage level will be considered to be moderate damage. It is worth noting that the above quantitative definition has certain universality for analyzing vulnerability of RC buildings, but further analysis and adjustment are needed for specific applications.

Table 6 merely presents the range of vulnerability in various states, and numerous impact cases exist within a same range. To assign specific of vulnerability to those diverse impact cases, we perform linear interpolation on vulnerability within the same interval, dependent on the inter-story displacement ratio, the velocity (v) and height (h) of particle flow, and the equation used for interpolation is demonstrated in Table 7. When the local damage is small, the inter-story displacement ratio is used to interpolate the vulnerability, while when the local damage is large, the vulnerability is obtained by the impact velocity and impact height of debris flow, which highlights the local damage effect of impact height and impact velocity on buildings. In the event of an impact disaster, the variation in particle flow density (ρ) is significantly less than the variation in impact velocity and impact height, therefore, we only take into account the influence of the latter two indictors. In the impact force variable of $\rho v^2 h$, we observe that when v and h increase by the same amount, the

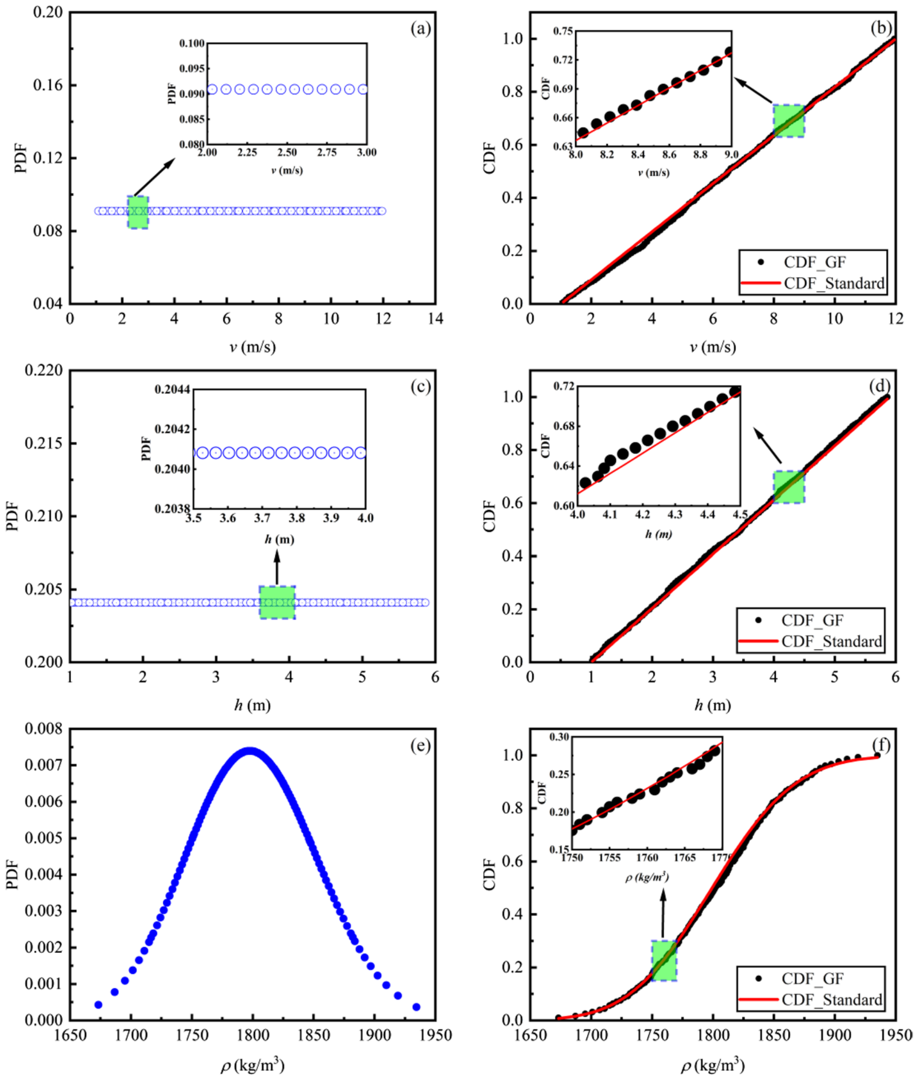

Fig. 9 Uniformly distributed samples selected using the generalized F-discrepancy (GF-discrepancy)-based method. **a**, **c**, and **e** PDFs and **b**, **d**, and **f** CDFs of the **a** and **b** velocity, **c** and **d** height, and **e** and **f** density of the flowing material

increment of impact force caused by v is greater than that caused by h. For convenience, the exponents of v and h in this variable are used to determine the contribution of v and h to vulnerability, resulting in a weight of approximately 2:1 for v and h. Accordingly, weights of 0.66 and 0.34 are assigned to the v and h. Using this method to assign specific vulnerability to each sample can help generate some relatively continuous points.

Table 6 Qualitative definition of the damage states of buildings

Damage state	Qualitative descriptions	Vulnerability (Kang et al. 2015)
Slight	Wall crack, and columns and beams remain intact or Minor nonstructural damage (Hu et al. 2012; Kang et al. 2015)	0–0.3
Moderate	The wall cracks and the beams and columns begin to break, but there is no risk of collapse (Mavrouli et al. 2014)	0.3–0.6
Heavy	The wall is broken, and the beams and columns are severely damaged, and the floor slab begins to fall off, posing a risk of collapse (Hu et al. 2012; Mavrouli et al. 2014)	0.6–0.8
Complete	50% of beam and column failures result in loss of bearing capacity and complete loss of maintenance value (Mavrouli et al. 2014; Luo et al. 2022)	0.8–1

6 Results

6.1 Vulnerability

Here, to intuitively present the impact results for over 100 samples, we constructed 6 vulnerability curves (Fig. 11) based on vulnerability value defined by Table 7. In the nonlinear regression analysis, Weibull distribution, a sigmoid function, was chosen for constructing vulnerability curves, due to the widespread use in characterizing the correlation between vulnerability and impact intensities of debris flow (Totschnig et al. 2013; Kang et al. 2015), and the basic mathematical notation of the function is shown in Table 8. The function established the relationships between the vulnerability and the flow depth h, flow velocity v, impact force measure hv^2, overturning moment measure hv, hydrodynamic impact pressure ρv^2, and relative intensity measure h/h_0, where h_0 is the height of the RC building. The final results were presented by the limit vulnerability curves (Green line) and suggested vulnerability curves (Red line), and the parameters used to fit the equation are shown in Table 8. Limit vulnerability curves, characterizing the maximum vulnerability value under the same impact intensity, were determined by fitting the points with the highest vulnerability in the figure. The suggested curves were obtained by fitting the average vulnerability (Red dots), which were weighted within a certain intensity range, assuming that the probabilities of each case are approximately equal.

A limit vulnerability index of 0.8 for the RC buildings can be determined given a flow depth of 2.36 m (Fig. 11a), a flow velocity of 4.10 m/s (Fig. 11b), a overturning moment measure of 21.8 m^2/s (Fig. 11c), an impact force measure of 99.81 m^3/s^2 (Fig. 11d), an impact pressure of 34.60 kPa (Fig. 11e), or a relative intensity of 0.43 (Fig. 11f). The proposed vulnerability index equals 0.8 for a flow depth of 4.57 m

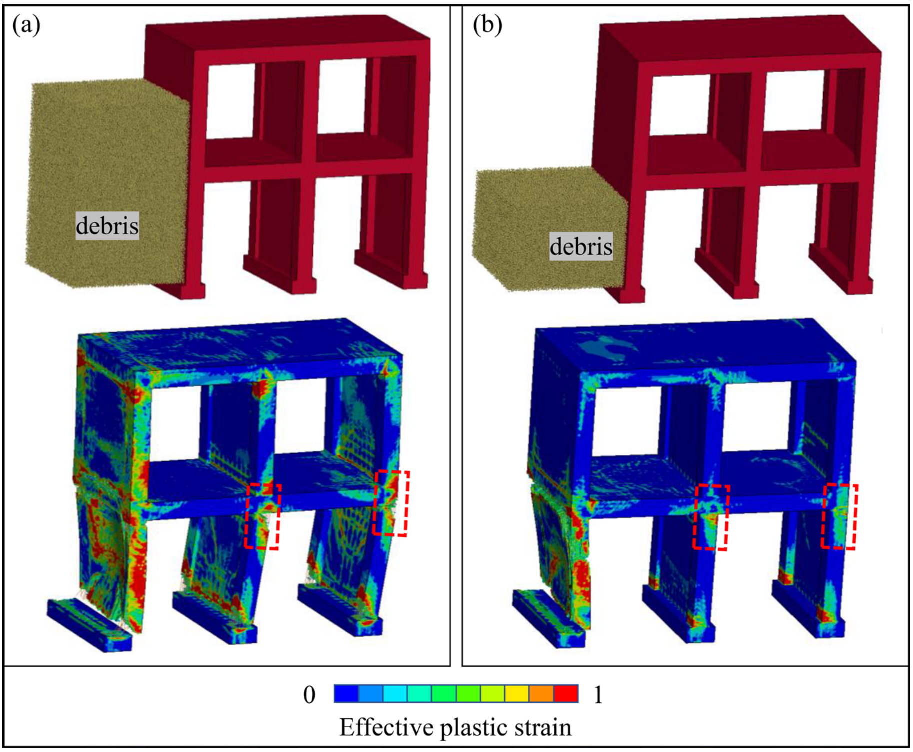

Fig. 10 Typical failure modes in the numerical simulations

(Fig. 11a), a flow velocity of 8.36 m/s (Fig. 11b), an overturning moment measure of 21.92 m^2/s (Fig. 11c), an impact force measure of 182.14 m^3/s^2 (Fig. 11d), an impact pressure of 157.16 kPa (Fig. 11e), or a relative intensity of 0.78 (Fig. 11f). Furthermore, in order to express the relationship between vulnerability and multivariate, a vulnerability surface fitted using polynomial regression and Tricube weighting method is presented, which is a function of independent variables of h and v, as shown in Fig. 12. Figure 12 demonstrates that the vulnerability surface is very smooth, indicating that our definition of the vulnerability has good continuity and, at the same time, to the greatest extent possible, overcomes the problem of having the same vulnerability value under different impact intensities. In addition, Fig. 12 highlights the spatial variation pattern of the vulnerability, intuitively reflecting the variation of the vulnerability with two-dimensional indicators and making it easier to apply to guide disaster assessments compared with a vulnerability curve.

6.2 Exceedance probability

After determining the damage status of each case, we divided every intensity indictor into several continuous intervals and calculated the probability of occurrence of the different

Table 7 Quantitative definition of the damage states of two-story reinforced concrete buildings

Quantitative description			Damage states	Vulnerability range	Value
Condition A	Condition B (m)				
Inter-story drift ratio of rear column (δ)	D_{wall}	D_{column}			
$\delta \leq 1/550$	< 0.001	< 0.01	Intact (L1)	0	0
	> 0.001		Slight (L2)	0–0.1	$f(\delta)$
		> 0.01	Moderate (L3)	0.3–0.35	$0.66f(v) + 0.34f(h)$
$1/550 < \delta \leq 1/100$		< 0.01	Slight (L2)	0.1–0.3	$f(\delta)$
		> 0.01	Moderate (L3)	0.35–0.4	$0.66f(v) + 0.34f(h)$
$1/100 < \delta \leq 1/50$		< 0.40	Moderate (L3)	0.4–0.6	$f(\delta)$
		> 0.40	Heavy (L4)	0.6–0.7	$0.66f(v) + 0.34f(h)$
$1/50 < \delta \leq 1/30$		< 0.40	Heavy (L4)	0.7–0.8	$f(\delta)$
		> 0.40	Complete (L5)	0.8–0.9	$0.66f(v) + 0.34f(h)$
$\delta > 1/30$			Complete (L5)	1	1

$f(\cdot)$ represents the linear interpolation function within the corresponding vulnerability interval and that $v \in [1, 5.9], h \in [1, 12]$

damage levels, namely, the damage probability P_{Li}, which was obtained by dividing the total number of cases in the same damage level by the total number of cases falling within same interval. Then, the exceedance damage probabilities of the different intensity indictors (hv, hv^2, Frh/h_0, and $Frhv/h_0v_0$, which were used by Luo et al. (2022)) were calculated using the equations listed in Table 9 with intervals of 3 m^2/s, 12 m^3/s, 0.1, and 0.15, respectively. In the expression of $Frhv/h_0v_0$, v_0 and F_r are the limit of the velocity in the study and the Froude number defined as $v/\sqrt{gh}$, that is, the ratio of the inertial force to the gravity. The exceedance damage probabilities of the different intensities are showed in Fig. 13. Because only one or two points fall within the intact state, fitting an accurate curve is difficult. Therefore, the exceedance probabilities of three levels of slight, moderate, and heavy damage are given here. The exceedance probability of 0.8 for the slight damage state occurs for threshold values of $hv = 16.5$ m^2/s (Fig. 13a), $hv^2 = 120$ m^3/s^2 (Fig. 13b), $Frh/h_0 = 0.57$ (Fig. 13c), and $Frhv/h_0v_0 = 0.34$ (Fig. 13d). The exceedance probability of 0.8 for the moderate damage state occurs for threshold values of $hv = 23.5$ m^2/s (Fig. 13a), $hv^2 = 180$ m^3/s^2 (Fig. 13b), $Frh/h_0 = 0.725$ (Fig. 13c), and $Frhv/h_0v_0 = 0.565$ (Fig. 13d). The exceedance probability of 0.8 for the heavy damage state occurs for threshold values of hv, hv^2, Frh/h_0, and $Frhv/h_0v_0$ equal to 30 m^2/s (Fig. 13a), 260 m^3/s^2 (Fig. 13b), 0.9 (Fig. 13c), and 0.8 (Fig. 13d), respectively. Compared with the hv indicator, the other three indicators have better fitting performances; that is, the discriminability of the exceedance probability of the hv indicator is not as good as those of the other three indicators when the evaluation sample is small.

6.3 Comparison

Here, we compare the proposed vulnerability curve with those from on-site investigations or simulations; the comparison results are shown in Fig. 14 and Table 10, where

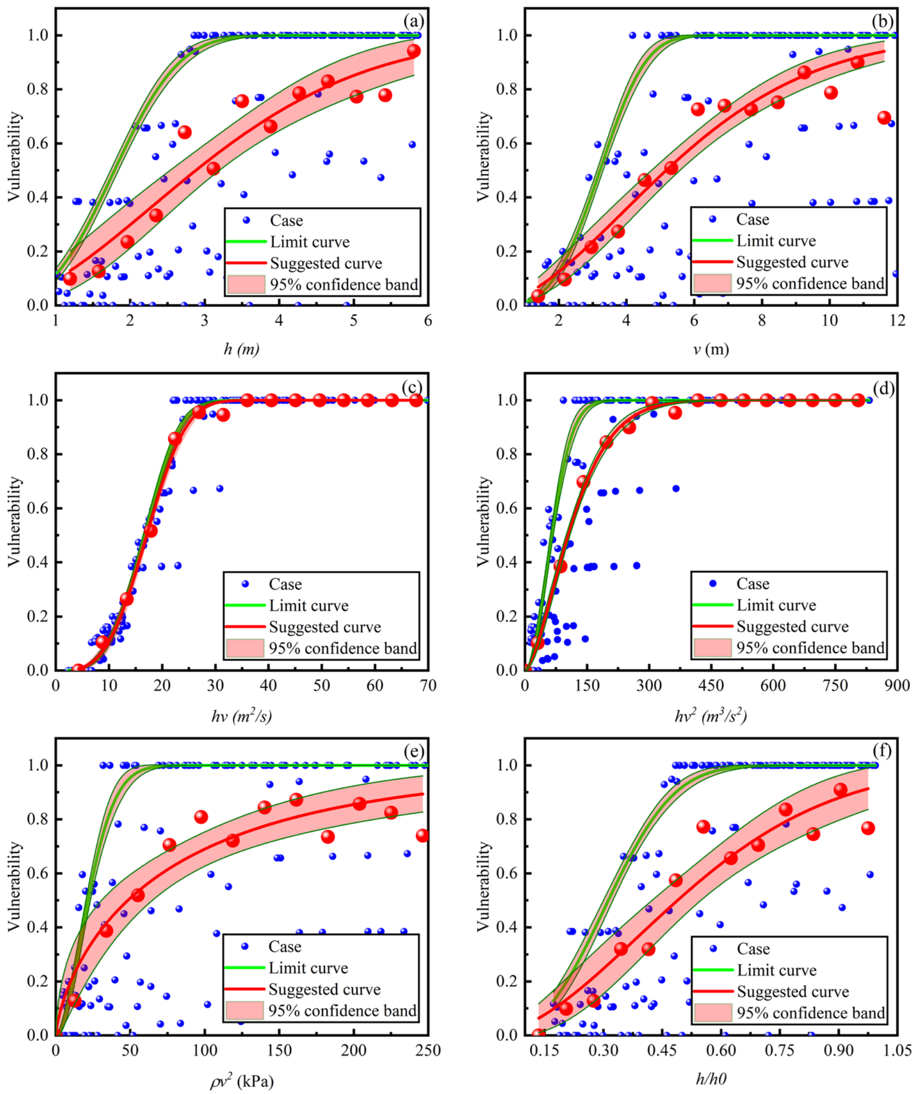

Fig. 11 Vulnerability curves for the reinforced concrete (RC) building

the broken lines represent the vulnerability of brick–concrete structures (Akbas et al. 2009; Quan Luna et al. 2011; Totschnig et al. 2013; Kang et al. 2015; Zhang et al. 2018) and the solid lines represent the vulnerability of RC buildings (Kang et al. 2015; Zhang et al. 2018). Overall, the limit vulnerability curve is approximately equal to or less than the vulnerability curve of the brick–concrete structures; the suggested vulnerability curves differ slightly from others' statistical results of the RC building (Fig. 14a–c). There are two primary reasons for the aforementioned phenomenon. On one hand, we added bars to the wall in building to enhance its resistance, thereby reducing its

Table 8 The parameters used to fit the vulnerability equation

Intensity index	Weibull distribution ($V = 1 - e^{(ax^b)}$)					
	Limit curve			Suggested curve		
	a	b	R^2	a	b	R^2
h	−1.21E-01	3.01	97.72%	−9.96E-02	1.83	91.52%
v	−1.24E-02	3.45	98.36%	−4.00E-02	1.74	96.72%
hv	−3.68E-05	3.50	98.46%	−5.19E-05	3.35	99.66%
hv^2	−2.23E-04	1.93	97.34%	−5.90E-04	1.52	99.77%
ρv^2	−2.83E-03	1.79	96.59%	−4.22E-02	0.72	91.81%
h/h_0	−1.67E+01	2.74	94.64%	−2.56E+00	1.83	91.73%

vulnerability. On the other hand, cases with low vulnerability were included in the suggested curves, leading to low vulnerability. Despite some deviations in the results, our suggested curves are close to the results of previous research, especially in Fig. 14a, which shows the effectiveness of our method.

In terms of specific intensity indicators, the threshold value of the impact intensity h (Fig. 14a) was compared with those of Zhang et al. (2018) and Kang et al. (2015); we found that the thresholds corresponding to a vulnerability of 0.8 for the Zhang et al. (2018), Kang et al. (2015), limit curve and suggested curve are 5.40 m, 4.36 m, 2.36 m, and 4.57 m, respectively. As for the intensity indictor v, Fig. 14b shows that, when v reaches 5.85 m/s, 6.46 m/s, 4.10 m/s, and 8.36 m/s for the Zhang et al. (2018), Kang et al. (2015), limit curve and suggested curve, the value of the vulnerability equals 0.8. Figure 14c illustrates that a vulnerability of 0.8 occurs when the impact pressures of the Zhang et al. (2018), Kang

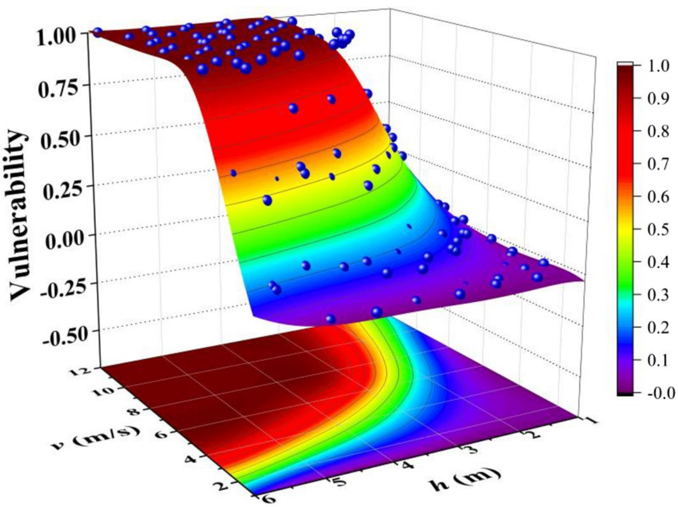

Fig. 12 Vulnerability surface for the RC building

et al. (2015), limit curve and suggested curve are 57.91 kPa, 121.17 kPa, 34.60 kPa, and 157.16 kPa, respectively. It can be observed in Fig. 14d that, when the vulnerability equals 0.8, the relative intensity corresponding to the Zhang et al. (2018) and limit curve are both 0.43, while the relative intensity is 0.78 for the suggested curve. Overall, our research results are closer to those of Kang et al. (2015), while there are significant differences from those of Zhang et al. (2018). These differences may arise from various aspects, such as the reinforcement ratio of the buildings, the building form, and the height of the building floors, and further studies of RC buildings under the impact of mass flows are required.

7 Discussion

The numerical simulation method used in this study has significant advantages when analyzing the vulnerability of buildings, providing an analytical tool for areas that have not experienced disasters but may in the future. However, the method has several shortcomings. First, although GF-discrepancy can effectively control the uniformity of the selected samples, extreme values are inevitably selected; such values may not occur in practical situations, leading to a bias in the vulnerability. Second, compared with vulnerability curves originating from statistical analyses containing the same type of architecture with various characteristics, this study only analyzed the vulnerability of a two-story RC building under debris avalanche impact. This method may be applicable to areas where the building form only changes slightly but is difficult to apply in areas with significant changes in the architectural structural form. If the vulnerability of other forms of buildings needs to be analyzed, re-modeling is necessary; this doubles the computational workload. Third, it may be difficult to analyze the results, such as those in Fig. 11, where the dispersion of the results makes it difficult to find a representative vulnerability curve; this problem has also been encountered by Luo et al. (2022).

8 Conclusions

According to the impact force of debris flows, this study considered three random variables, namely, the impact height, impact velocity, and density of the mass flow, which were sampled via GF-discrepancy to obtain a total of 134 cases. Then, a deterministic analysis was performed on these cases using the DEM-FEM coupling method to find the responses of the inter-story drift ratio and the displacement of the walls and columns. On the basis of these responses, we conducted a vulnerability analysis on a two-story RC building and drew the following conclusions.

Table 9 Equations used to calculate the exceedance probability

Damage state	Intact	Slight	Moderate	Heavy
Damage probability	P_{L1}	P_{L2}	P_{L3}	P_{L4}
Exceeding damage probability	$1-P_{L1}$	$1-\sum_{i=1}^{2} P_{Li}$	$1-\sum_{i=1}^{3} P_{Li}$	$1-\sum_{i=1}^{4} P_{Li}$

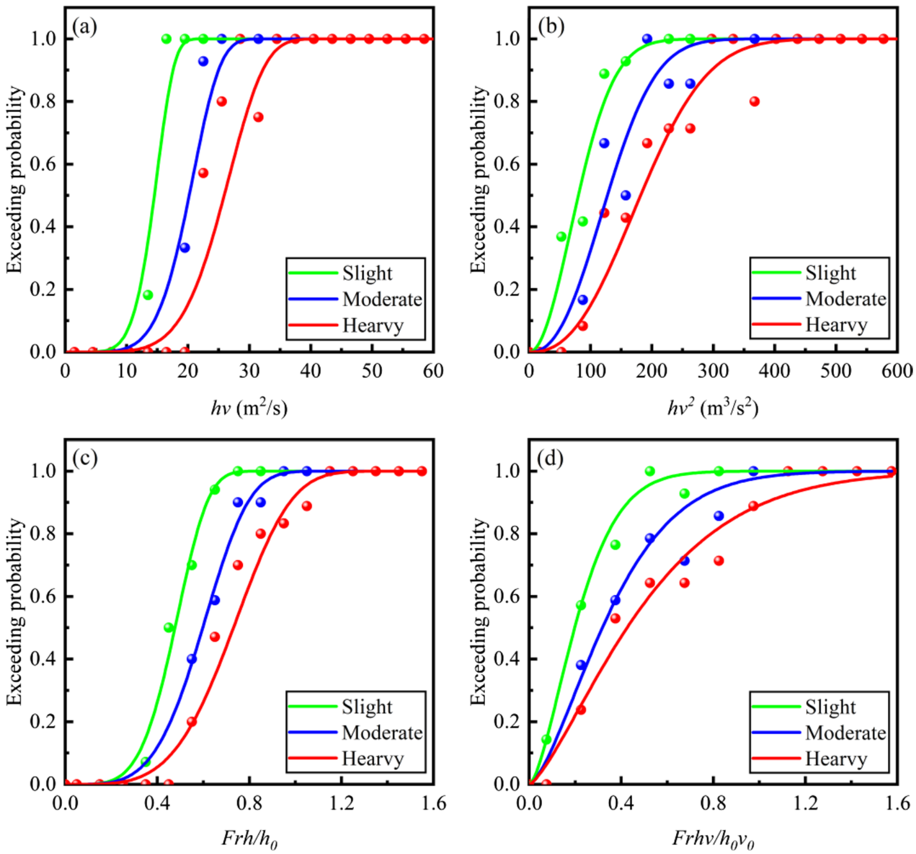

Fig. 13 Exceedance probability of the RC building characterized by different intensity indicators

(1) DEM can be well coupled with FEM, fully describing the interaction and damage process between debris avalanches and buildings. Meanwhile, the GF-discrepancy-based point selection method can generate relatively uniform samples, to a great extent avoiding vulnerability bias and redundant calculations caused by sample point concentration. The proposed method can provide a reference for vulnerability analyses of areas that have not yet been impacted by debris avalanches but may be impacted in the future.

(2) Within the framework of qualitative vulnerability descriptions, this study proposed three quantitative vulnerability assessment indictors for two-story RC buildings: the inter-story drift ratio and the displacement of the walls and columns. The vulnerability surface indicates that the vulnerability defined by this set of indicators has good continuity in the space determined by the intensity of the impact height and the impact velocity.

(3) In this study, we provided both the ultimate vulnerability curves and the recommended vulnerability curves for RC buildings based on the equal weight method corresponding to six impact intensity indicators. The limit vulnerability curves are close to or

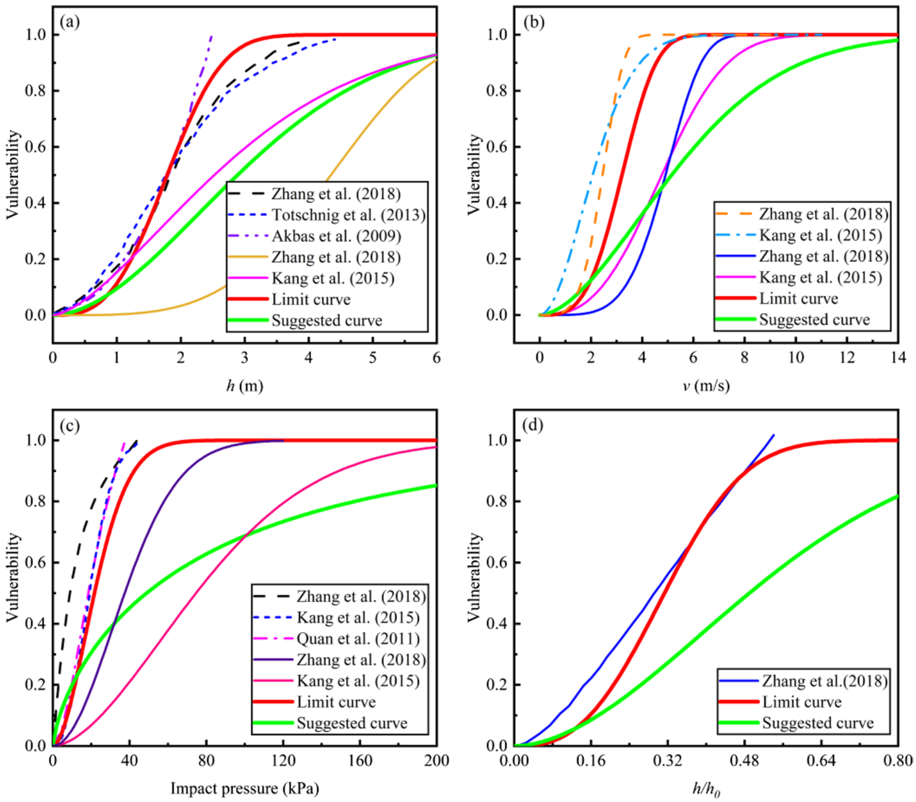

Fig. 14 Comparison of the vulnerability functions for the RC building with other studies. The broken and solid lines indicate the vulnerability curves of the brick–concrete structures and the RC buildings, respectively

Table 10 Threshold of the intensity indictors corresponding to a vulnerability of 0.8 for RC buildings

Intensity indictors	Threshold (Vulnerability = 0.8)			
	Zhang et al. (2018)	Kang et al. (2015)	Limit curve	Suggested curve
Impact height (m)	5.40	4.36	2.36	4.57
Impact velocity (m/s)	5.85	6.46	4.10	8.36
Impact pressure (kPa)	57.91	121.17	34.60	157.16
Relative intensity		0.43	0.43	0.78

smaller than that of brick–concrete structures, and there are small differences between the recommended vulnerability curves and those of previous studies on RC buildings. Overall, the final results show that the method proposed in this paper is effective.

Author contributions The first draft of the manuscript was written by JP. YH contributed to the study conception and design. The pictures drawn by ZG and YB. CX, XL and ZC jointly completed the revision of the manuscript. All authors read and approved the final manuscript.

Funding This study was supported by the National Natural Science Foundation of China (No. 41831291).

Declarations

Conflict of interest The authors declared that they have no conflicts of interest to this work.

References

Akbas S, Blahut J, Sterlacchini S (2009) Critical assessment of existing physical vulnerability estimation approaches for debris flows. pp 229–233
Albaba A, Lambert S, Kneib F, Chareyre B, Nicot F (2017) DEM modeling of a flexible barrier impacted by a dry granular flow. Rock Mech Rock Eng 50(11):3029–3048
Cai W, Zhu H, Liang W (2022a) Three-dimensional stress rotation and control mechanism of deep tunneling incorporating generalized Zhang-Zhu strength-based forward analysis. Eng Geol 308:106806
Cai W, Zhu H, Liang W (2022b) Three-dimensional tunnel face extrusion and reinforcement effects of underground excavations in deep rock masses. Int J Rock Mech Min Sci 150:104999
Casagli N, Intrieri E, Tofani V, Gigli G, Raspini F (2023) Landslide detection, monitoring and prediction with remote-sensing techniques. Nat Rev Earth Environ 4(1):51–64
Chen JB, Chan JP (2019) Error estimate of point selection in uncertainty quantification of nonlinear structures involving multiple nonuniformly distributed parameters. Int J Numer Meth Eng 118(9):536–560
Chen JB, Zhang SH (2013) Improving point selection in cubature by a new discrepancy. SIAM J Sci Comput 35(5):A2121–A2149
Chen JB, Yang JY, Li J (2016) A GF-discrepancy for point selection in stochastic seismic response analysis of structures with uncertain parameters. Struct Saf 59:20–31
Chen M, Tang CA, Zhang XZ, Xiong J, Chang M, Shi QY, Wang FL, Li MW (2021) Quantitative assessment of physical fragility of buildings to the debris flow on 20 August 2019 in the Cutou gully, Wenchuan, southwestern China. Eng Geol 293:106319
Chen K, Pang R, Xu B (2023) Stochastic dynamic response and seismic fragility analysis for high concrete face rockfill dams considering earthquake and parameter uncertainties. Soil Dyn Earthq Eng 167:107817
Cheng HL, Chen ZY, Huang Y (2022) Quantitative physical model of vulnerability of buildings to urban flow slides in construction solid waste landfills: a case study of the 2015 Shenzhen flow slide. Nat Hazards 112(2):1567–1587
Code for seismic design of buildings (2016) Beijing, China architecture & building press. GB 50011-2010: pp 1–510
Feng SJ, Gao HY, Gao L, Zhang LM, Chen HX (2019) Numerical modeling of interactions between a flow slide and buildings considering the destruction process. Landslides 16(10):1903–1919
Froude MJ, Petley DN (2018) Global fatal landslide occurrence from 2004 to 2016. Nat Hazard 18(8):2161–2181
Hu KH, Cui P, Zhang JQ (2012) Characteristics of damage to buildings by debris flows on 7 August 2010 in Zhouqu Western China. Nat Hazards Earth Syst Sci 12(7):2209–2217. https://doi.org/10.5194/nhess-12-2209-2012
Huang D, Li YQ, Song YX, Xu Q, Pei XJ (2019) Insights into the catastrophic Xinmo rock avalanche in Maoxian County, China: combined effects of historical earthquakes and landslide amplification. Eng Geol 258:105158
Jiang YJ, Towhata I (2013) Experimental study of dry granular flow and impact behavior against a rigid retaining wall. Rock Mech Rock Eng 46(4):713–729
Kang H-S, Kim Y-T (2015) The physical vulnerability of different types of building structure to debris flow events. Nat Hazards 80(3):1475–1493
Kappes MS, Papathoma-Kohle M, Keiler M (2012) Assessing physical vulnerability for multi-hazards using an indicator-based methodology. Appl Geogr 32(2):577–590
Karajan N, Han Z, Teng H, Wang J (2014) On the parameter estimation for the discrete-element method in LS-DYNA®. In: 13th International LS-DYNA users conference, pp 1–9

Kim MI, Kwak JH (2020) Assessment of building vulnerability with varying distances from outlet considering impact force of debris flow and building resistance. Water 12(7):2021
Ko FWY, Lo FLC (2018) From landslide susceptibility to landslide frequency: a territory-wide study in Hong Kong. Eng Geol 242:12–22
Li J, Chen J (2017) Some new advances in the probability density evolution method. Appl Math Mech 38(1):32–43
Li J, Wang D (2023) Comparison of PDEM and MCS: accuracy and efficiency. Probab Eng Mech 71:103382
Liang YZ, Xiong F (2019) Quantification of debris flow vulnerability of typical bridge substructure based on impact force simulation. Geomat Nat Haz Risk 10(1):1839–1862
Liu C, Yu Z, Zhao S (2019) Quantifying the impact of a debris avalanche against a flexible barrier by coupled DEM-FEM analyses. Landslides 17(1):33–47
Liu C, Yu ZX, Zhao SC (2021) A coupled SPH-DEM-FEM model for fluid-particle-structure interaction and a case study of Wenjia gully debris flow impact estimation. Landslides 18(7):2403–2425
Liu C, Phuong N, Zhao S (2022) Dynamic response of reinforced concrete sheds against the impact of rock block with different shapes and angles. Can J Civ Eng 49(6):870–884
Luo HY, Zhang LL, Zhang LM (2019) Progressive failure of buildings under landslide impact. Landslides 16(7):1327–1340
Luo H, Zhang L, Wang H, He J (2020) Multi-hazard vulnerability of buildings to debris flows. Eng Geol 279:105859
Luo HY, Zhang LM, Wang HJ, He J (2021) Process of building collapse caused by the Po Shan Road landslide in Hong Kong on 18 June 1972. Landslides 18(12):3769–3780
Luo HY, Zhang LM, He J, Yin KS (2022) Reliability-based formulation of building vulnerability to debris flow impacts. Can Geotech J 59(1):40–54
Mavrouli O, Fotopoulou S, Pitilakis K, Zuccaro G, Corominas J, Santo A, Cacace F, De Gregorio D, Di Crescenzo G, Foerster E, Ulrich T (2014) Vulnerability assessment for reinforced concrete buildings exposed to landslides. Bull Eng Geol Environ 73:265–289. https://doi.org/10.1007/s10064-014-0573-0
Murray YD (2007) Users manual for LS-DYNA concrete material model 159. Computer Program Documentation
Papathoma-Köhle M, Keiler M, Totschnig R, Glade T (2012) Improvement of vulnerability curves using data from extreme events: debris flow event in South Tyrol. Nat Hazards 64(3):2083–2105
Papathoma-Köhle M, Gems B, Sturm M, Fuchs S (2017) Matrices, curves and indicators: A review of approaches to assess physical vulnerability to debris flows. Earth Sci Rev 171:272–288
Parisi F, Sabella G (2017) Flow-type landslide fragility of reinforced concrete framed buildings. Eng Struct 131:28–43
Petley D (2012) Global patterns of loss of life from landslides. Geology 40(10):927–930
Prieto JA, Journeay M, Acevedo AB, Arbelaez JD, Ulmi M (2018) Development of structural debris flow fragility curves (debris flow buildings resistance) using momentum flux rate as a hazard parameter. Eng Geol 239:144–157
Qingyun Z, Mingxin Z, Dan H (2022) Numerical simulation of impact and entrainment behaviors of debris flow by using SPH–DEM–FEM coupling method. Open Geosci 14(1):1020–1047
Quan Luna B, Blahut J, van Westen CJ, Sterlacchini S, van Asch TWJ, Akbas SO (2011) The application of numerical debris flow modelling for the generation of physical vulnerability curves. Nat Hazard 11(7):2047–2060
Ren X, Liang YP, Feng DC (2022) Fragility analysis of a prestressed concrete containment vessel subjected to internal pressure via the probability density evolution method. Nucl Eng Design 390:111709
Shi CL, Zhang JG, Zhang JB, Shao F, Zhang YC, Zhang ML (2021) Experimental study and numerical analysis on impact resistance of civil air defense engineering shear wall. Adv Civ Eng 2021:1–20
Shields MD, Zhang JX (2016) The generalization of Latin hypercube sampling. Reliab Eng Syst Saf 148:96–108
Tang HM, Wasowski J, Juang CH (2019) Geohazards in the three gorges reservoir area, China lessons learned from decades of research. Eng Geol 261:105267
Thouret JC, Antoine S, Magill C, Ollier C (2020a) Lahars and debris flows: characteristics and impacts. Earth Sci Rev 201:103003
Thouret JC, Antoine S, Magill C, Ollier C (2020b) Lahars and debris flows: characteristics and impacts. Earth Sci Rev 201:103003
Totschnig R, Fuchs S (2013) Mountain torrents: quantifying vulnerability and assessing uncertainties. Eng Geol 155:31–44
Yan S, He S, Deng Y, Liu W, Wang D, Shen F (2020) A reliability-based approach for the impact vulnerability assessment of bridge piers subjected to debris flows. Eng Geol 269:105567

Yang J, Tao J, Sudret B, Chen J (2019) Generalized F-discrepancy-based point selection strategy for dependent random variables in uncertainty quantification of nonlinear structures. Int J Numer Meth Eng 121(7):1507–1529
Yin YP, Li B, Wang WP, Zhan LT, Xue Q, Gao Y, Zhang N, Chen HQ, Liu TK, Li AG (2016) Mechanism of the december 2015 catastrophic landslide at the shenzhen landfill and controlling geotechnical risks of urbanization. Engineering 2(2):230–249
Yu J, Dong Z, Yu J, Liu F, Ye J, Dong F (2022) Dynamic response of masonry walls strengthened with engineered cementitious composites under simulated debris flow. J Struct Eng 148(9):04022113
Yuen TY, Weng MC, Fu YY, Lu GT, Shiu WJ, Lu CA, GeoPORT Working Group (2023) Assessing the impact of rockfall on a bridge by using hybrid DEM/FEM analysis: a case study in Central Taiwan. Eng Geol 314:107000
Zhang JQ, Gurung DR, Liu RK, Murthy MSR, Su FH (2015) Abe Barek landslide and landslide susceptibility assessment in Badakhshan Province. Afghan Landslides 12(3):597–609
Zhang S, Zhang LM, Li XY, Xu Q (2018) Physical vulnerability models for assessing building damage by debris flows. Eng Geol 247:145–158
Zhong H, Yu Z, Zhang C, Lyu L, Zhao L (2022) Dynamic mechanical responses of reinforced concrete pier to debris avalanche impact based on the DEM-FEM coupled method. Int J Impact Eng 167:104282

Publisher's Note Springer Nature remains neutral with regard to jurisdictional claims in published maps and institutional affiliations.

Springer Nature or its licensor (e.g. a society or other partner) holds exclusive rights to this article under a publishing agreement with the author(s) or other rightsholder(s); author self-archiving of the accepted manuscript version of this article is solely governed by the terms of such publishing agreement and applicable law.